

PHOTOEVAPORATION OF PROTOSTELLAR DISKS. V. CIRCUMSTELLAR DISKS UNDER THE INFLUENCE OF BOTH EXTREME-ULTRAVIOLET AND FAR-ULTRAVIOLET RADIATION

SABINE RICHLING^{1,2} AND HAROLD W. YORKE²

Received 1999 October 5; accepted 2000 March 17

ABSTRACT

The evolution and appearance of protostellar disks can be significantly altered by their UV environment. We investigate numerically the photoevaporation of protostellar disks under the influence of an external radiation field with both EUV ($h\nu > 13.6$ eV) and FUV ($6 \text{ eV} < h\nu < 13.6$ eV) components. Our two-dimensional axisymmetric radiation hydrodynamics calculations begin with star-disk configurations resulting from previously published collapse simulations. We follow the evolution after the external UV radiation source has been turned on. We consider the transfer of both direct (from the UV point source) as well as diffuse radiation fields simultaneously with the ionization of hydrogen and carbon. A simplified cooling function is employed which assumes that the carbon ionization front separates the molecular region from the region in atomic or ionized form. For some simulations an isotropic stellar wind has been included at the position of the disk's central star. At selected evolutionary times a frequency-dependent ray-tracing diagnostic code is used to calculate emission line spectra and emission line maps over the volume of interest. The interaction of the FUV-induced neutral flow at the disk surface with the direct and diffuse EUV radiation fields leads to the typical head-tail objects with bright emission line crescents and tails pointing away from the external radiation source. The properties of the head-tail objects are in agreement with the properties of the proplyds in the Orion Nebula, M8, NGC 2024, and—in a more extreme UV environment—of the newly discovered proplyds in NGC 3603. After losing material via photoevaporation over a time $\gtrsim 10^5$ yr, our initially rather massive disks are reduced to typical observed disk masses. At this time the radius of the disk, the radius of the hydrogen ionization front, and the length of the tail are compatible to observed proplyds. Our model disks can be either silhouetted or nonsilhouetted in the emission line maps, depending on orientation. The [O III] 5007 Å emission appears more diffuse than [O II] 3726 Å, because the abundance of O III is low near the hydrogen ionization front and in the shadow regions along the tail. Monopolar and bipolar microjets emerging from the proplyds can be explained by spherically symmetric stellar winds hydrodynamically focused by the neutral evaporating flow from the disk surface.

Subject headings: circumstellar matter — hydrodynamics — H II regions — line: formation — radiative transfer — stars: formation

1. INTRODUCTION

The occurrence of disks around young stars and protostars is a common feature in star-forming regions. Circumstellar disks are detected by direct imaging around low-mass (Padgett et al. 1999), intermediate-mass (Mannings & Sargent 2000), and high-mass stars (Cesaroni et al. 1999), in binary systems (Close et al. 1998; Stapelfeldt et al. 1998), and in more evolved gas-poor or gas-less stages (Körner et al. 1998). Circumstellar disks are continually evolving; they dissipate due to various processes such as viscous accretion, close stellar encounters and stellar winds. If significant ultraviolet radiation is available, photoevaporation is the dominant disk dispersal mechanism (Hollenbach, Yorke, & Johnstone 2000). Whereas disks of high-mass stars are photoevaporated by the central star, disks of young low-mass stars are subject to photoevaporation by nearby massive stars and/or to some extent by their own X-rays from hot coronae.

Examples for externally ionized protostellar disks are the well-studied objects in the Orion Nebula (O'Dell, Wen, &

Hu 1993; McCaughrean & Stauffer 1994; Chen et al. 1998; Bally et al. 1998a). These objects, commonly referred to as proplyds (PROtoPLANetarY Disks), are interpreted as the ionized envelopes of young star-disk systems. In optical emission lines (H α , [O III], [N II]) they appear as bright heads with tails pointing away from the major ionizing source θ^1 Ori C. Some of them contain dark silhouettes which match the [O I] and H₂ emission and probably trace the surface of an embedded optically thick disk. Infrared images show the presence of central stars in most of the proplyds. The detection of similar objects in M8 (Stecklum et al. 1998), NGC 3603 (Brandner et al. 1999), and NGC 2024 (Stapelfeldt et al. 2000, in preparation) suggests that photoevaporation by an external star is an important process for the evolution of circumstellar disks.

The appearance of proplyds can be explained by the interaction of EUV ($h\nu > 13.6$ eV) and FUV ($6 \text{ eV} < h\nu < 13.6$ eV) radiation from an external source with a circumstellar disk. FUV photons are absorbed principally by dust and penetrate much deeper into the disk than their higher energy counterparts. At relative high column densities they dissociate molecules, heat the material virtually impenetrable to the EUV photons, and initiate a neutral flow away from the disk. This “photon-dominated region” (PDR; also known as “photodissociation region”) is encased within a hydrogen ionization front (I-front), where

¹ Institut für Theoretische Astrophysik, Tiergartenstr. 15, D-69121 Heidelberg, Germany.

² MS 169-506, Jet Propulsion Laboratory, California Institute of Technology, Pasadena, CA 91109.

the outflowing PDR material can be ionized by the EUV photons. The flow is not spherically symmetric. The resulting quasi-equilibria between (1) the ram pressure of the neutral flow and the pressure of the ionized material and (2) the flux of EUV photons into the I-front and the flux of neutral material across the I-front together with (3) the deflection of material flow away from the external source lead to a complex nonuniform density structure and a “head-tail” shape of the I-front. Depending on the ratio of the FUV/EUV photon fluxes, the hydrogen I-front can stand off at a considerable distance from the disk surface, appearing as a bright round head in the direction of the illuminating source with an extended “cometary” tail of lower emissivity on the far side of the disk.

Johnstone, Hollenbach, & Bally (1998) presented analytical and numerical models for the structure of such neutral flows. Depending on the radius of the disk, the flux of EUV and FUV photons and the column of neutral gas in the PDR, the neutral flow can either be EUV-dominated or FUV-dominated. In EUV-dominated flows the PDR is geometrically thin and the flux of EUV photons determines the mass-loss rate. In FUV-dominated flows the PDR consists of a supersonic wind region and a thick subsonic layer separated by a shock front. The mass-loss rate is determined by the FUV photon flux. Störzer & Hollenbach (1999) improved these models by including the results of equilibrium and nonequilibrium PDR codes to calculate the column density and temperature inside the PDR. They determined under which circumstances FUV-dominated flows are possible and conclude that the observed sizes of the ionization fronts of many proplyds in the Orion Nebula can be explained by FUV-dominated flows. From the resulting mass-loss rates, an assumed surface density distribution, and an illumination timescale equal to the age of the Orion star-forming region (10^5 – 10^6 yr; Hillenbrand 1997), they calculated disk masses which are consistent with the observed disk masses ($< 0.02 M_{\odot}$; Bally et al. 1998b).

The models of Johnstone et al. (1998) and Störzer & Hollenbach (1999) assume a steady state spherical flow emerging from a spherical clump and do not determine the density and flow structure self-consistently with the thermal structure and the radiation field. By contrast, we use a fully self-consistent two-dimensional radiation hydrodynamics code and follow the evolution of a star-disk system after an external UV radiation source has switched on. Due to the two-dimensional setup and an improved treatment of diffuse radiation fields, it is possible to examine the photoevaporation flow at the top, the edge, and the back side of the disk, the redirection of material from the head into the tail, and the evolution of the disk and the tail itself. Shocks appear as a natural consequence of the interacting flows. A ray-tracing procedure is employed to calculate isophote maps for various emission lines, allowing a demonstrative comparison with observations. This work is a continuation of our previous work, where only the EUV radiation was considered (Richling & Yorke 1998). Here we present the results obtained with an extended code which includes the effects of FUV radiation within the framework of a simplified PDR model.

In § 2 we give a short introduction to the radiation hydrodynamics code. In § 3 we present the PDR model and describe the necessary modifications to the code. The star-disk models and the parameters of the calculations are described in § 4. In §§ 5 and 6 we present the results of the

radiation hydrodynamical simulations and of the diagnostic ray-tracing code. Finally, we give a summary of our results in § 7.

2. THE RADIATION HYDRODYNAMICS CODE

Many features of the physical model and the numerical procedures used in the two-dimensional radiation hydrodynamics code are described in the previous papers of this series (Yorke & Welz 1996; Richling & Yorke 1997, 1998). The code solves the hydrodynamical equations in cylindrical coordinates on self-similar nested grids (Yorke & Kaisig 1995). This allows us to numerically resolve the disk well, especially close to the central star, while covering a large volume of space. Self-gravity and an α -viscosity (Shakura & Sunyaev 1973) are included. The transfer of EUV and FUV photons is calculated along lines of sight centered at the star outside the computational domain. The external UV source is freely relocatable along the rotation axis of the system. The dust temperature is determined by a continuum radiation transfer module which employs the gray flux-limited diffusion (FLD) approximation (Levermore & Pomraning 1981; Yorke & Kaisig 1995). The FLD approximation is also used to calculate the three diffuse UV radiation fields: soft EUV photons ($h\nu \sim 14$ eV), resulting from recombinations of hydrogen into the ground state, and EUV as well as FUV photons, resulting from scattering on dust grains. The most important heating and cooling contributions in H II regions and PDRs are considered. In the following we describe the FUV related physics in detail.

3. THE PDR MODEL

PDRs contain all of the atomic and most of the molecular gas and are often modeled analytically and numerically (see, e.g., review by Hollenbach & Tielens 1997). One-dimensional models usually consider complex chemical networks to calculate the temperature structure and the abundances of various atomic and molecular species. In two-dimensional simulations including radiation transfer it would be far too time-consuming to include such elaborate chemical networks. Consequently, some simplifying assumptions must be made.

Our PDR model is shown schematically in Figure 1. A circumstellar disk is illuminated by EUV and FUV photons. EUV photons ionize hydrogen until they reach the hydrogen ionization front (H I-front). The H II region is heated principally by the excess energy of electrons ejected during photoionization of hydrogen and cooled by forbidden line radiation of N II, O II, and O III. FUV photons penetrate deeper into the medium until they reach the carbon ionization front (C I-front). We assume that between the H and C I-fronts the material consists of atomic hydrogen and singly ionized “metals” with ionization potentials below 13.6 eV. Behind the C I-front the material is molecular, i.e., the C I-front and the dissociation fronts are assumed to coincide. Within the PDR the major heating mechanism is photoejection of electrons from dust grains; the gas is cooled by fine-structure line emission of O I and C II.

This approximation is well justified for the current problem. The gas density at the border of the disk increases by about 2 orders of magnitude within 3–4 grid cells. The C I-front lies exactly within this region and has approx-

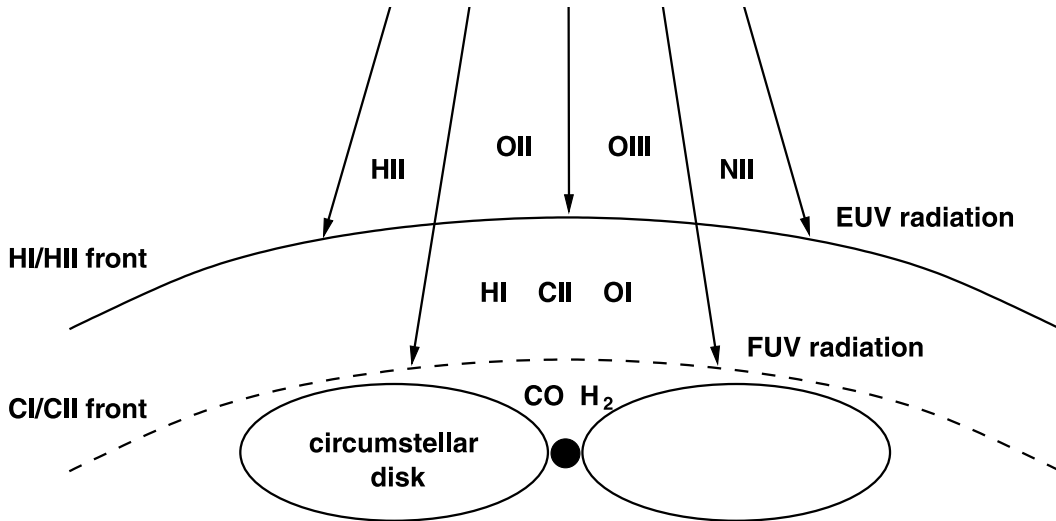


FIG. 1.—PDR model. A circumstellar disk is illuminated by EUV photons ($h\nu > 13.6$ eV) and FUV photons ($6 \text{ eV} < h\nu < 13.6$ eV). EUV photons ionize hydrogen until they reach the H I-front. FUV photons penetrate the H I-front and reach the C I-front close to the disk surface. Our models assume that the material is molecular behind the C I-front and atomic or ionized (depending on the ionization potential) between the C I-front and the H I-front.

imately the same width. Plane-parallel models for dense equilibrium PDRs (Sternberg & Dalgarno 1995) and non-equilibrium PDRs (Störzer & Hollenbach 1998) show that the C I-front and the dissociation fronts of H_2 and CO are usually colocated within a column density of about 1 order of magnitude. We thus expect that these fronts practically coincide within the limited resolution of our numerical grid. The large drop of the temperature behind the C I-front is another plausible reason to use it as the boundary between the warm PDR gas and the cool disk material (Johnstone & Bertoldi 1998). Of course, certain species appear predominantly in narrow zones between the C I-front and the dissociation fronts. Thus, a more careful treatment—beyond the scope of the present investigation—would be necessary to resolve the emission features of these species.

3.1. UV Photon Rates

The EUV and FUV photon rates S_{EUV} and S_{FUV} of the external radiation source are estimated from an assumed luminosity L and effective temperature T_{eff} :

$$S_{\text{EUV}} = \frac{\int_0^\infty B_\nu(T_{\text{eff}})/h\nu d\nu}{\int_0^\infty B_\nu(T_{\text{eff}}) d\nu} \times L, \quad (1)$$

$$S_{\text{FUV}} = \frac{\int_0^{\nu_{\text{FUV}}} B_\nu(T_{\text{eff}})/h\nu d\nu}{\int_0^\infty B_\nu(T_{\text{eff}}) d\nu} \times L \times \gamma, \quad (2)$$

where B_ν is the Planck function, $h\nu_{\text{EUV}} = 13.6$ eV, and $h\nu_{\text{FUV}} = 6$ eV. The three parameters L , T_{eff} , and the dimensionless factor γ in equation (2) allow us to vary the magnitude, hardness, and FUV/EUV ratio of the UV photon rates independently in order to investigate parameter space.

3.2. Transfer of Direct FUV Photons

The FUV photon density $u_{\text{direct}}^{\text{FUV}}$ from direct stellar illumination is calculated along lines of sight centered at the external source by solving the equation

$$u_{\text{direct}}^{\text{FUV}} = \frac{S_{\text{FUV}}}{4\pi d^2 c} \exp(-\tau_{\text{FUV}}), \quad (3)$$

with the FUV optical depth

$$\tau_{\text{FUV}} = \int [n_{\text{C}}(1 - x_{\text{C}})\sigma_{\text{C}}^{\text{FUV}} + \rho\kappa^{\text{ext}}] ds. \quad (4)$$

We consider extinction due to ionization of carbon and dust extinction. n_{C} and x_{C} are the particle density and degree of ionization of carbon, respectively. $\sigma_{\text{C}}^{\text{FUV}}$ is the photoionization cross section of carbon averaged over the FUV photon spectrum between 11.26 eV < $h\nu$ < 13.6 eV. The specific dust extinction coefficient or gram-opacity κ^{ext} depends on the abundance and the composition of the dust grains. Dust models (Draine & Lee 1984; Preibisch et al. 1993) propose values in the range of $\kappa^{\text{ext}} \sim$ several tens to several hundreds $\text{cm}^2 \text{g}^{-1}$. In the vicinity of protostellar disks small grains should be depleted due to sedimentation, coagulation, and sputtering in shocks which leads to a lower FUV extinction coefficient (Suttner, Yorke, & Lin 1999). We choose $\kappa^{\text{ext}} = 300 \text{ cm}^2 \text{g}^{-1}$.

3.3. Diffuse FUV Radiation

The diffuse FUV photon density $u = u_{\text{dust}}^{\text{FUV}}$ resulting from scattering on dust grains is determined by solving the flux-limited diffusion equation

$$\frac{\partial u}{\partial t} - \nabla \cdot \left(\frac{\lambda c}{\chi^{\text{ext}}} \nabla u \right) = \epsilon - \chi^{\text{abs}} c u, \quad (5)$$

where the flux-limiter λ is given by

$$\lambda = \frac{1}{R} \left(\coth R - \frac{1}{R} \right) \text{ with } R = \frac{|\nabla u|}{\chi^{\text{ext}} u}. \quad (6)$$

Emission rate ϵ , extinction coefficient χ^{ext} and absorption coefficient χ^{abs} are calculated from

$$\epsilon = \rho \kappa^{\text{scat}} c u_{\text{star}}^{\text{FUV}}, \quad (7)$$

$$\chi^{\text{ext}} = n_{\text{C}}(1 - x_{\text{C}})\sigma_{\text{C}}^{\text{FUV}} + \rho \kappa^{\text{ext}}, \quad (8)$$

$$\chi^{\text{abs}} = n_{\text{C}}(1 - x_{\text{C}})\sigma_{\text{C}}^{\text{FUV}} + \rho \kappa^{\text{abs}}. \quad (9)$$

TABLE 1
CIRCUMSTELLAR DISK MODELS (FROM YORKE & BODENHEIMER 1999)

Model	M_{star} (M_{\odot})	L_{star} (L_{\odot})	$T_{\text{dust}}^{\text{c}}$ (K)	M_{disk} (M_{\odot})	R_{disk} (1000 AU)	t_{disk} (10^3 yr)	$t_{\text{disk}}/t_{\text{ff}}$	Numerical Grid $N_{\text{G}} \times N_{\text{Z}} \times N_{\text{R}}$	X_{max} (1000 AU)	ΔX_{min} (AU)
I.....	0.58	3.68	150	0.40	1.0	215	2.2	$4 \times 244 \times 122$	6.82	6.85
II.....	0.66	17.1	932	0.35	0.18	27.0	3.1	$5 \times 116 \times 58$	1.34	1.44
III.....	1.14	11.3	398	0.90	1.7	438	2.2	$6 \times 116 \times 58$	13.5	7.28

NOTES.— M_{star} , mass of the central star; L_{star} , luminosity of the central star; $T_{\text{dust}}^{\text{c}}$, central dust temperature; M_{disk} , disk mass; R_{disk} , disk radius; t_{disk} , disk age in 10^3 yr and in free-fall times t_{ff} ; N_{G} , level of grid nesting; $N_{\text{Z}} \times N_{\text{R}}$, number of cells per grid level; X_{max} , the extension of the coarsest grid in radial and $\pm Z$ directions; ΔX_{min} , resolution of the finest grid.

We assume isotropic scattering with a specific dust scattering coefficient $\kappa^{\text{scat}} = 200 \text{ cm}^2 \text{ g}^{-1}$. The specific dust absorption coefficient is calculated from $\kappa^{\text{abs}} = \kappa^{\text{ext}} - \kappa^{\text{scat}}$.

3.4. Ionization/Recombination of Carbon

The degree of ionization of carbon x_{C} is determined by solving the time-dependent rate equation

$$\frac{\partial x_{\text{C}}}{\partial t} = (1 - x_{\text{C}})[\sigma_{\text{C}}^{\text{FUV}} u^{\text{FUV}} + \sigma_{\text{C}}^{\text{EUV}} u^{\text{EUV}}]c - \alpha_{\text{C}} x_{\text{C}} n_{\text{e}}. \quad (10)$$

Here u^{EUV} and u^{FUV} are the sums of all direct and diffuse EUV and FUV photon densities. $\sigma_{\text{C}}^{\text{EUV}}$ is the photoionization cross section of carbon averaged over the EUV photon spectrum. The total recombination coefficient

$$\alpha_{\text{C}} = 3.74 \times 10^{-12} \left(\frac{T}{300 \text{ K}} \right)^{-0.5} \quad (11)$$

is taken from Bertoldi (2000). It is an approximation for gas temperatures between $T = 10\text{--}10^4$ K of the results obtained by Nahar & Pradhan (1994), including both radiative and dielectronic recombination of carbon. The electron density $n_{\text{e}} = nx + n_{\text{C}} x_{\text{C}}$ consists of contributions from the ionization of hydrogen and carbon, where x is the degree of ionization of hydrogen and n the total particle density.

3.5. Heating

The major heating mechanism in PDRs is photoelectric ejection of electrons from grains. The corresponding

heating function depends on composition, size distribution, and charge of the dust grains. Bakes & Tielens (1994) numerically determined a heating rate in dependence on the gas temperature T , the electron density n_{e} , and the FUV flux G_0 in Habing units ($H = 1.6 \times 10^3 \text{ ergs cm}^{-2} \text{ s}^{-1}$) for $T_{\text{eff}} = 30,000$ K. We use their analytical approximation of the heating rate

$$\Gamma = 10^{-24} \eta G_0 n \text{ ergs s}^{-1}, \quad (12)$$

with the heating efficiency

$$\eta = \frac{3 \times 10^{-2}}{1 + 2 \times 10^{-4} T^{0.5} G_0 / n_{\text{e}}}, \quad (13)$$

and the correction factor obtained by Spaans et al. (1994) for different T_{eff} .

3.6. Cooling

The cooling in PDRs is dominated by collisional excitation of fine structure lines. We consider the most important lines [C II] 158 μm , [O I] 63 μm , and [O I] 145 μm and use the escape probability formalism according to Tielens & Hollenbach (1985) to calculate the cooling rate of a transition from level i to level j

$$\Lambda = n_i A_{ij} h\nu_{ij} \beta_{\text{esc}}(\tau_{ij}), \quad (14)$$

where n_i is the population density of the upper level obtained by solving the corresponding rate equations. A_{ij} is the spontaneous transition probability, and $h\nu_{ij}$ is the

TABLE 2
PARAMETERS FOR THE CASES CALCULATED

Case	Model	d (10^{17} cm)	L ($10^6 L_{\odot}$)	$\log S_{\text{EUV}}$ (s^{-1})	$\log S_{\text{FUV}}$ (s^{-1})	γ	$\log f_{\text{EUV}}$ ($\text{cm}^{-2} \text{ s}^{-1}$)	$\log f_{\text{FUV}}$ ($\text{cm}^{-2} \text{ s}^{-1}$)	v_{wind} (km s^{-1})	$\log \alpha$
A.....	I	3.08	0.147	48.86	49.25	1	12.8	13.2	5	−6
B.....	I	1.54	0.147	48.86	49.25	1	13.4	13.8	5	−6
C.....	I	1.05	0.147	48.86	49.25	1	13.7	14.1	5	−6
D.....	I ^a	1.54	0.147	48.86	49.25	1	13.4	13.8	100	−6
E.....	I ^a	1.54	0.147	48.86	49.25	1	13.4	13.8	200	−6
F.....	II	1.54	0.147	48.86	49.25	1	13.4	13.8	5	−6
G.....	II	1.54	0.147	48.86	49.25	1	13.4	13.8	5	−2
H.....	III	40.1	20.2	51.00	51.38	1	12.7	13.1	5	−6
J.....	III	40.1	20.2	51.00	52.09	5	12.7	13.8	5	−6

NOTES.—Starting models from Table 1; d , distance of ionizing star from disk's center; L , luminosity of ionizing star; S , UV photon rates of ionizing star; γ , dimensionless factor to change the FUV/EUV flux ratio (see eq. [2]); $f = S/4\pi d^2$, photon fluxes at the disk's center; v_{wind} , velocity of the wind originating from the disk's central star; α , parameter for angular momentum transfer. The effective temperature is the same in all simulations $T_{\text{eff}} = 38,500$ K.

^a Simulation starts with model I of case A at $t = 59.3 \times 10^3$ yr.

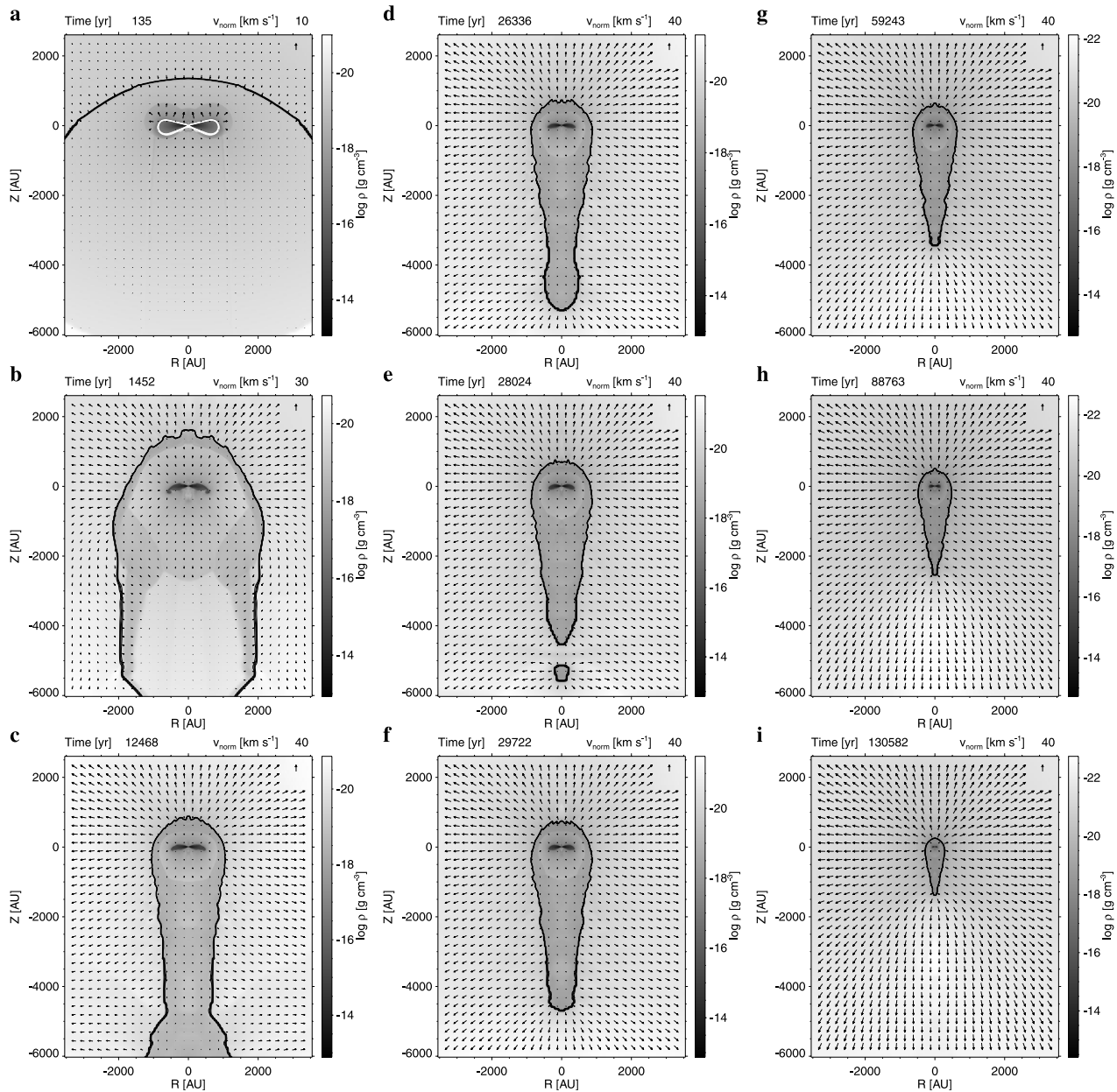


FIG. 2.—Evolution of star-disk system I under the influence of an external EUV and FUV radiation field (case A). The gray scale represents the density structure and the arrows the velocity field. The black lines are contour lines of constant degree of ionization of hydrogen and are given for $x = 0.2, 0.4, 0.6$, and 0.8 . Their concentration shows that the H I-front is indeed a discontinuity. The white lines in the first picture are contour lines of constant degree of ionization of carbon x_c and are given for the same values as for x , thus illustrating the C I-front discontinuity. For clarity these contours are not shown at later evolutionary times.

energy difference between level i and j . The escape probability $\beta_{\text{esc}}(\tau_{ij})$ is calculated using a formula given by de Jong, Dalgarno, & Boland (1980). The optical depth of the line τ_{ij} is determined by integrating along a different set of lines of sight as described in § 3.2. Here the lines of sight start at the boundary cells of the numerical grid and are centered at the position of the star within the disk. Although the lines of sight are not always perpendicular to the surface of the disk, this procedure should provide an approximation for τ_{ij} , which is adequate for our purposes.

4. INITIAL CONDITIONS

4.1. Star-Disk Models

The starting models are circumstellar disk systems

resulting from collapse simulations of 1 and $2 M_{\odot}$ molecular clumps (Yorke & Bodenheimer 1999). Since the collapse code employs the same numerical techniques, we are able to follow self-consistently the evolution of a low-mass system within a star-forming cluster. Switching on the external UV source means that the star-disk system either comes into contact with an existing H II region or is suddenly illuminated by a new-born massive star nearby.

The characteristic parameters of the models are summarized in Table 1. The luminosity L_{star} of the protostar with mass M_{star} is the sum of an intrinsic stellar luminosity and an accretion luminosity. The radius of the disk R_{disk} is defined by its sudden decrease in density of about 2 orders of magnitude and depends on the initial conditions of the parental molecular clump. Models I and III evolved from a

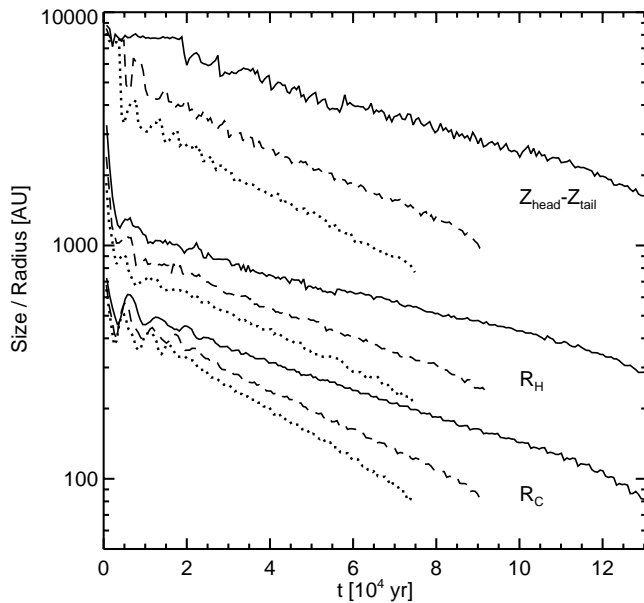


FIG. 3.—Evolution of the size of the head-tail object in Z-direction ($Z_{\text{head}} - Z_{\text{tail}}$), the radial width of the H I-front R_H and the radial width of the C I-front R_C at the equatorial plane for simulations A (solid lines), B (dashed lines), and C (dotted lines).

rather extended molecular clump with a radius approximately equal to the extension of the coarsest grid X_{max} . Their disks have radii $R_{\text{disk}} \sim 10^3$ AU. Model II evolved from a less extended molecular clump and has a disk with a much smaller radius ($R_{\text{disk}} = 180$ AU) and with better spatial resolution within the innermost grid. The evolutionary age t_{disk} of the models is in the range of two to three free-fall times.

4.2. The Calculations

The two-dimensional simulations of the evolution of star-disk systems under the influence of EUV and FUV radiation require a huge amount of CPU time and depend on the choice of a large set of free parameters. Because it is impossible to examine this multidimensional parameter space fully, we used observationally related setups and varied some of the parameters in order to test their influence on the evolution.

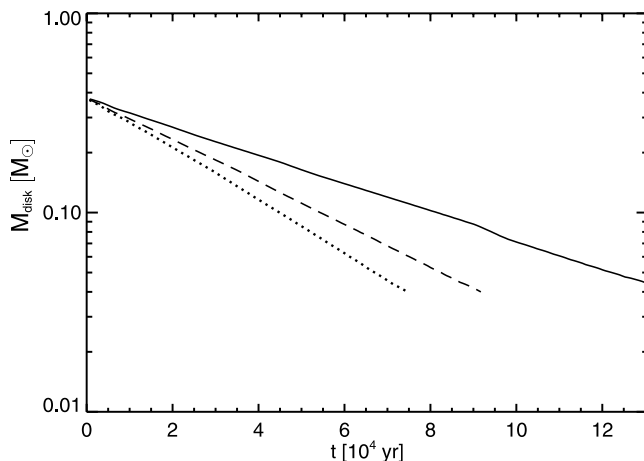


FIG. 4.—Evolution of the disk mass M_{disk} in simulations A (solid line), B (dashed line), and C (dotted line).

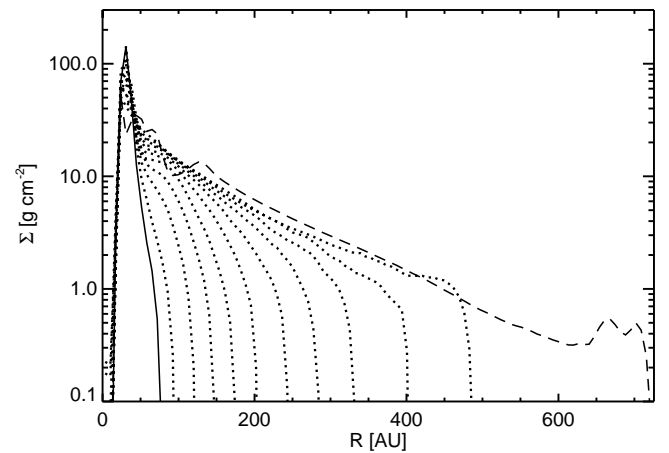


FIG. 5.—Evolution of the surface density Σ in simulation A. Σ is given near the beginning of the simulation (dashed lines, $t = 720$ yr), at the end of the simulation (solid line, $t = 13 \times 10^4$ yr), and at several intermediate stages (dotted lines, $\Delta t \sim 1.3 \times 10^4$ yr).

Table 2 shows the parameters of the calculated cases. Simulations A to G examine the situation of the proplyds in the Orion Nebula: The EUV and FUV photon rates resemble those of the main ionizing source in the Trapezium Cluster. The distances d between the star-disk system and the external source are in the range of 0.1 and 0.025 pc which are typical values for the Orion proplyds (Bally et al. 1998a). Cases H and J simulate the evolution of star-disk system III illuminated by a cluster of O stars and were originally intended to model the recently detected proplyds in NGC 3603 (Brandner et al. 1999). Since the photon fluxes at the disk's center are comparable to simulations A to G, the results of cases H and J can also be applied to the Orion proplyds, except for the minor effect that the lines of sight are more nearly parallel at the disk's position. For the simulations with initial conditions I and III the calculations are stopped when the radial extent of the disk falls below 10 grid cells on the finest grid.

5. RESULTS

5.1. General Evolution (Case A)

The evolution of star-disk system I in case A is displayed in Figure 2. The gray scale represents the density structure and the arrows show the velocity field. The black contour lines for the degree of ionization of hydrogen mark the position of the H I-front separating the hot ionized gas from the warm PDR material. The external radiation source is located at $d = 0.1$ pc above the disk. The upper left frame (Fig. 2a) shows the very early structure of the system: 10^2 yr after the sudden onset of the external radiation source the C I-front (white contour lines) already envelops the densest parts of the disk. FUV photons heat the gas to temperatures up to 5000 K and launch a neutral flow above the disk expanding with a supersonic velocity. The H I-front approaching from the top is still unaffected by the presence of the disk.

Approximately 10^3 yr later (Fig. 2b), diffuse FUV photons have established a neutral flow below the disk, and the disk is embedded in a wind-blown bubble of neutral gas. The bubble is confined by a shock front with a radius R_S , which is about twice as large as the radius of the disk defined by the radius of the C I-front R_C . The disk itself is

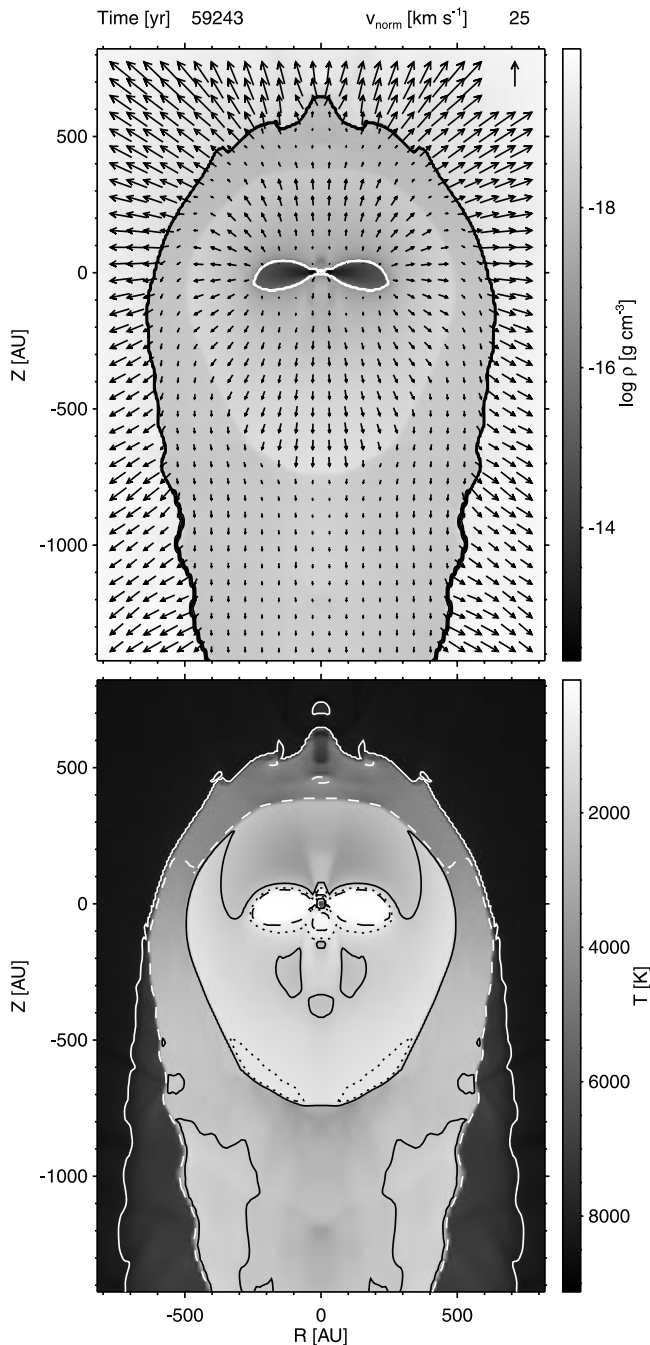


FIG. 6.—Head of the object in case A at $t = 59,243$ yr (Fig. 2g). *Top*: Density, velocity, and degree of ionization of hydrogen and carbon. *Bottom*: Gas temperature T . The contour lines correspond to $T = 500$ K (black dashed line), 1000 K (black dotted line), 2000 K (black solid line), 4000 K (white dashed line), and 8000 K (white solid line).

considerably disturbed at its outer edge. This phenomenon also occurred in our earlier simulations (Richling & Yorke 1998), which considered the effects of EUV only. Due to the asymmetrical EUV radiation field the disk was gradually truncated to a radius where the gas pressure in the disk compensates the external pressure. Here the distortion is caused by the asymmetrical FUV radiation field. In Figure 2b the H I-front compresses the neutral flow beyond the bubble to a thick layer of subsonic gas. Below the disk the movement of the H I-front is determined by the diffuse EUV radiation fields. After 10^4 yr (Fig. 2c) a clear head-tail

configuration has developed. The head of the object has reached a quasi-steady state discussed below. At this point in time the tail is still evolving and has attained a length Z_{tail} greater than the extension of the numerical grid.

The middle row of Figure 2 shows the tail evolution after the H I-front has closed on the numerical grid. Evaporated material from the back side of the disk and redirected material from the head accumulates in the tip of the tail leading to a broad tail end (Fig. 2d). Induced by instabilities at the H I-front a globule of warm PDR material breaks off from the tail (Fig. 2e). The instabilities arise because the thin ionized gas compresses a denser and cooler gas (Rayleigh-Taylor instability) and because of the tangential velocities at the PDR side of the H I-front (Kelvin-Helmholtz instability). The instabilities cause wavelike disturbances in the H I-front which are recognizable at all times. In Figure 2f the object is displayed shortly after the globule left the computational domain with the evaporating flow. Again material accumulates in the tip of the tail. The periodic departing of globules in simulation A occurs a few times between $t = 2 \times 10^4$ yr and $t = 7 \times 10^4$ yr. The globules have masses of less than $10^{-5} M_{\odot}$ and evaporate in less than 10^3 yr. These processes may explain the observed irregularities at the tail tips of the Orion proplyds.

The long-term evolution of the head-tail object is shown in Figures 2g–2i. The object maintains its general form but shrinks considerably. Figure 3 shows this behavior more quantitatively. The evolution of the radial extent of the C I-front R_C and of the H I-front R_H in the equatorial plane and the total length of the object in the Z-direction ($Z_{\text{head}} - Z_{\text{tail}}$) are shown as solid lines. Over the course of 13×10^4 yr the radius of the disk R_C has decreased from initially ~ 1000 to 80 AU. The decrease of $R_H \sim 2 \dots 4 \times R_C$ is less steep. The ratio of the total length in the Z-direction to the total width of the object $(Z_{\text{head}} - Z_{\text{tail}})/2R_H$ evolves from ~ 4 to ~ 3 . At the end of the evolution (Fig. 2i) the object has an H I-front width $2R_H = 560$ AU and length ~ 1600 AU. Due to the exponential decrease of R_C the evolution of the mass of the disk exhibits a similar behavior (Fig. 4, solid line). The time in which the disk mass shrinks to $1/e$ of its initial value is the evaporation timescale $t_{\text{evap}} = 6.1 \times 10^4$ yr. The evolution of the surface density of the disk is displayed in Figure 5. The disk is photoevaporated from the outside in. The outer parts of the disk are more strongly affected than the central parts; the slope of the surface density increases during the evolution.

In Figure 6 the head of the object in simulation A at $t = 59,243$ yr (Fig. 2g) is displayed in greater detail. The C I-front (white contour lines) tightly envelops the cool disk material ($T < 100$ K). The PDR between the C I-front and the H I-front shows the structure of a FUV-dominated flow as described by Störzer & Hollenbach (1999): A shock front separates the freely expanding neutral flow from a thick subsonic layer. The neutral flow accelerates due to pressure gradients and reaches velocities of $v_{\text{max}} \sim 10 \text{ km s}^{-1}$ before it is shocked. The pressure gradients result from the spherical divergence of the flow and from a mildly negative temperature gradient in the outer more tenuous region of the supersonic flow. v_{max} is of order 1–2 times the sound speed in this region ($T = 2000\text{--}4000$ K) and therefore consistent with the estimate of Johnstone et al. (1998). The density and gas temperature in the subsonic layer behind the shock front is fairly constant in the direction of the flow. Assuming momentum conservation in a spherically sym-

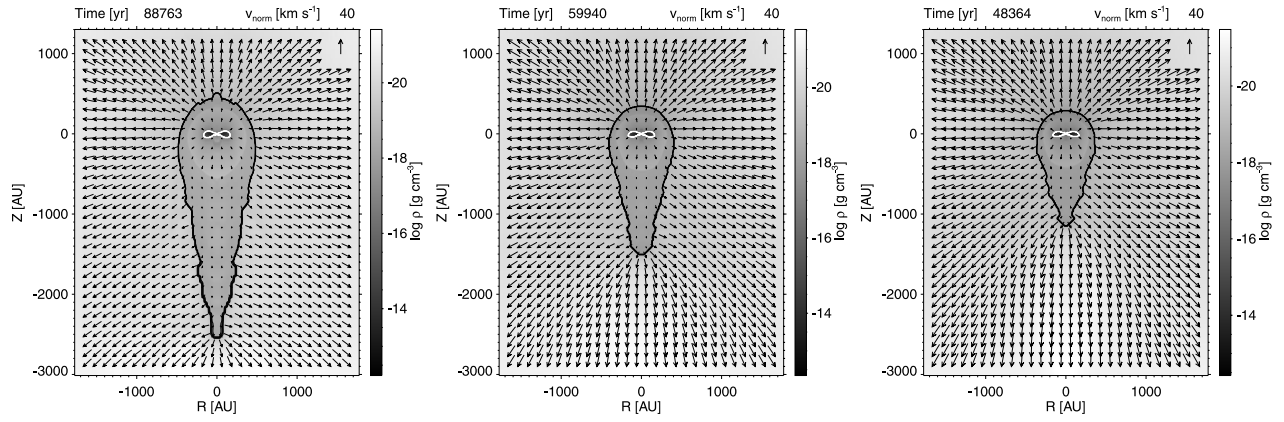


FIG. 7.—Density and velocity structure of the head-tail objects in simulations A, B, and C at evolutionary times when the radius of the disk R_C is equal in all three cases.

metric flow and a D-critical H I-front, the position of the shock front R_S can be calculated from

$$\frac{R_S}{R_H} = \sqrt{\frac{v_{\max}}{2c_{HII}}} \sim 0.7, \quad (15)$$

where c_{HII} is the sound speed within the H II region (Johnstone et al. 1998). This result is in good agreement for the position of the shock front above and at the edge of the disk. The radius of the shock front below the disk and the tail length are determined by the diffuse UV fields.

In the subsonic layer material is redirected from the head into the tail. Due to the redirection both the density and gas temperature within this layer decrease from above the disk to the edge of the disk. The redirection rate in the equatorial plane is of order several $10^{-7} M_{\odot} \text{ yr}^{-1}$, which is $\sim 20\%$ of the mass-loss rate from the disk surface facing the external star; i.e., 80% of the neutral disk material escapes directly through the H I-front. Johnstone & Bertoldi (2000) first estimated the redirection rate $\dot{M}_{\text{red}} = An_{\text{sub}}c_{\text{sub}}$ in a subsonic shell with constant number density n_{sub} and sound speed c_{sub} . $A = \pi(R_H^2 - R_S^2)$ is the cross section of the shell in the equatorial plane. They concluded that approximately 50% of the evaporated material would be redirected toward the tail. But using a smaller cross section (with $R_S/R_H \sim 0.7$ instead of 0.5) and considering

the drop in density and sound speed, their analysis would lead to a fraction of redirected material more consistent with our numerical results.

5.2. Influence of UV Flux (Cases B and C)

For cases B ($d = 0.05$ pc) and C ($d = 0.034$ pc) the distance between the circumstellar disk and the external star is smaller than for case A ($d = 0.1$ pc) but the evolution is very similar. The main difference is a more rapid evolution of the tail because of the more intense EUV fields. Departing neutral globules were not recognizable in the data sets sampled every ~ 700 yr. Figure 7 displays the head-tail objects in simulations A, B, and C at evolutionary times for which the disk radii R_C are approximately equal. With decreasing distance the radius of the H I-front R_H and the geometrical thickness of the neutral layer, as well as the size of the object ($Z_{\text{head}} - Z_{\text{tail}}$) decrease (see also Fig. 3). For cases B and C the mass of the disk decreases more rapidly than for case A (Fig. 4). The corresponding values for the evaporation timescale t_{evap} are given in Table 3.

The flow within the PDR head is a FUV-dominated flow for all times in all cases. For a specific dust extinction coefficient $\kappa^{\text{ext}} = 500 \text{ cm}^2 \text{ g}^{-1}$ and a preshock velocity $v_{\max} = 3 \text{ km s}^{-1}$ Störzer & Hollenbach (1999) predict FUV-dominated flows for FUV fluxes in the range of $5 \times 10^4 < G_0 < 2 \times 10^7$ and disk radii between $10 \text{ AU} < R_C < 100 \text{ AU}$. For higher v_{\max} and for lower κ^{ext} FUV-dominated flows are possible for much larger R_C . These results are consistent with our simulations: We use a specific dust extinction coefficient $\kappa^{\text{ext}} = 300 \text{ cm}^2 \text{ g}^{-1}$, calculate preshock velocities $v_{\max} \sim 10 \text{ km s}^{-1}$, and obtain FUV-dominated flows for disks with radii of several 100 AU. In

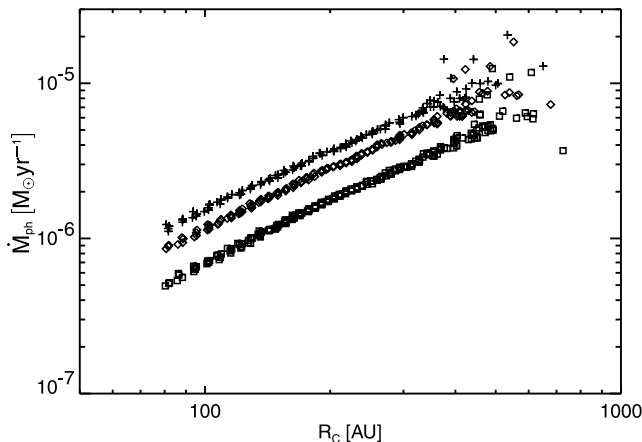


FIG. 8.—Photoevaporation rate \dot{M}_{ph} as a function of the radius of the C I-front R_C for case A (squares), case B (diamonds), and case C (crosses).

TABLE 3

PARAMETER FITS FOR PHOTOEVAPORATION RATES

Case	t_{evap} (10^4 yr)	\dot{M}_{100} ($10^{-6} M_{\odot} \text{ yr}^{-1}$)	δ
A.....	6.1	0.70	1.32
B.....	4.1	1.16	1.27
C.....	3.3	1.55	1.23

NOTES.— t_{evap} , evaporation timescale; \dot{M}_{100} and δ , results of a power-law fit of the form $\dot{M}_{\text{ph}} = \dot{M}_{100}(R_C/100 \text{ AU})^{\delta}$ for the dependence of the photoevaporation rate \dot{M}_{ph} on the radius of the C I-front.

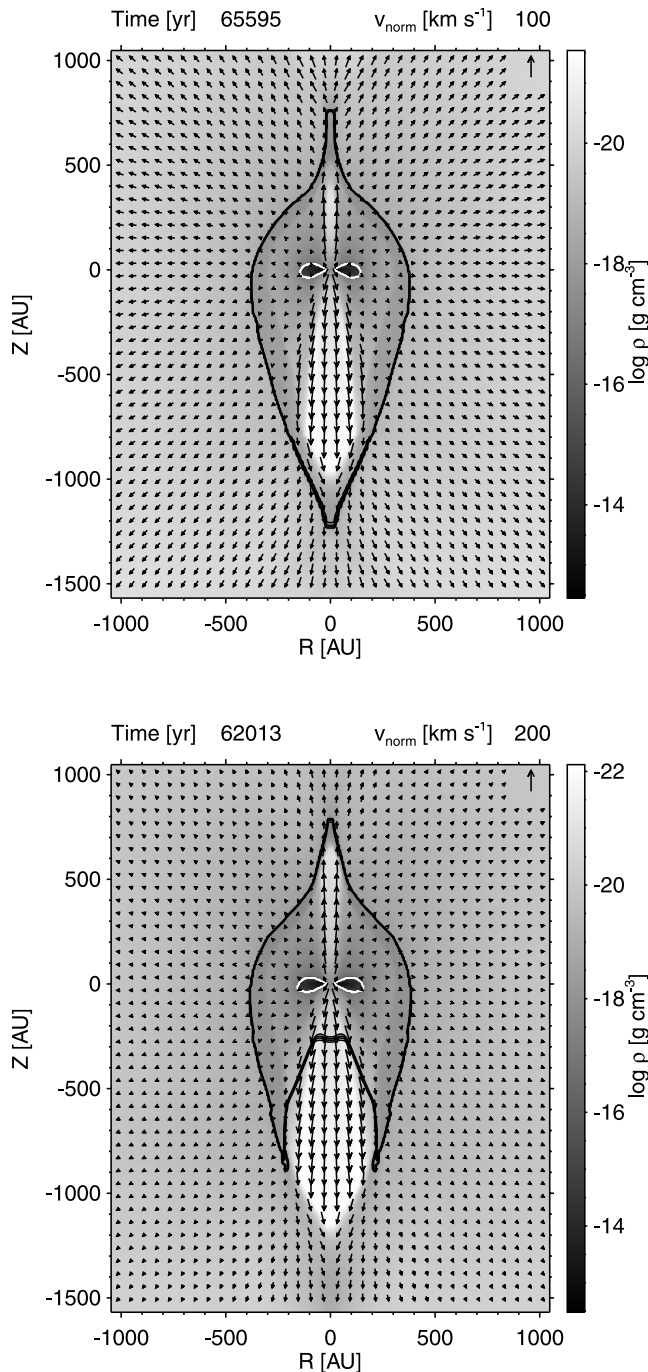


FIG. 9.—Density and velocity structure of the model at the end of simulations D ($v_{\text{wind}} = 100 \text{ km s}^{-1}$) and E ($v_{\text{wind}} = 200 \text{ km s}^{-1}$). The mass-loss rate of the stellar wind is $\dot{M}_{\text{wind}} = 2 \times 10^{-7} M_{\odot} \text{ yr}^{-1}$ in both cases.

our simulations the FUV fluxes are in the range $10^5 < G_0 < 10^6$.

The dependence of the photoevaporation rate \dot{M}_{ph} on the radius of the disk R_C is shown in Figure 8 for case A, B, and C. According to Johnstone et al. (1998) \dot{M}_{ph} is given by the particle density n_0 and the flow speed v_0 at the base of the flow integrated over a spherical clump with radius r_0

$$\dot{M}_{\text{ph}} = 4\pi r_0^2 n_0 v_0. \quad (16)$$

In FUV-dominated flows the optical depth is dominated by dust extinction $\tau_{\text{FUV}} \sim \int \kappa^{\text{ext}} \rho ds$. In this case the gas column density in the PDR ($\tau \sim 1$) is $N_{\text{H}} \sim 10^{21} \text{ cm}^{-2}$ (500

$\text{cm}^2 \text{ g}^{-1}/\kappa^{\text{ext}}$). If the supersonic flow region dominates the column density, then $N_{\text{H}} \sim n_0 r_0$ and $\dot{M}_{\text{ph}} \propto r_0$. Fitting the numerical results to a power law of the form

$$\dot{M}_{\text{ph}} = \dot{M}_{100} \left(\frac{R_C}{100 \text{ AU}} \right)^{\delta}, \quad (17)$$

yields an exponent $\delta = 1.23\text{--}1.32$ (Table 3), which is in agreement with the results of Störzer & Hollenbach (1999), who find $\dot{M} \sim 10^{-7} M_{\odot} \text{ yr}^{-1} (r_0/100 \text{ AU})^{1-1.5}$ for $d \approx 0.2 \text{ pc}$ (Hollenbach et al. 2000). In our simulations the value of \dot{M}_{100} is almost an order of magnitude higher because d and κ^{ext} are lower. Also, the neutral subsonic layer contributes significantly to the total column density. Due to redirection of material from the head into the tail this contribution is smaller at the edge of the disk, leading to a higher value for n_0 and consequently to a higher value for \dot{M}_{ph} . In the simulations the contribution of the subsonic layer to the total column density is 10%–30% directly above the disk and 5%–15% at the edge.

The size of the objects at the end of the simulations (see Fig. 3) are comparable to the observations. The proplyds in the Orion Nebula have H I-front widths between 44 and 1720 AU and lengths between 200 and 1600 AU. The ratio of the H I-front radius divided by the semimajor axis of the dark silhouette ranges from about 1.5 to 4 (Bally et al. 1998a). Disk masses derived from observations at 1.3 mm (Bally et al. 1998b) yield $M_{\text{disk}} \lesssim 0.02 M_{\odot}$. In the simulations the mass of the disk would reach this limit after $t \gtrsim 10^5 \text{ yr}$. Taken at face value this would imply that, because we are able to observe the proplyds of Orion, we must be living at a very lucky time. Since, however, the disks are assumed to be on circular orbits ($d = \text{constant}$) and are always illuminated face-on, our calculated evaporation timescales t_{evap} are lower limits. Even for FUV-dominated flows the photoevaporation rate depends on the distance to the illuminating star (Fig. 8). For the case of radial orbits Hollenbach et al. (2000) point out that each proplyd in the Trapezium Cluster has passed close to $\theta^1 \text{ Ori C}$ only once, reducing the timescale with high mass loss significantly. Hence, our numerical results are consistent with an illumination timescale of $\sim 10^6 \text{ yr}$, the estimated age of $\theta^1 \text{ Ori C}$.

5.3. Influence of Stellar Wind (Cases D and E)

Simulations D and E start with the model of case A at $t = 59.3 \times 10^3 \text{ yr}$ (Fig. 2g). For case D the stellar wind velocity is gradually increased to a velocity $v_{\text{wind}} = 100 \text{ km s}^{-1}$ and for case E to $v_{\text{wind}} = 200 \text{ km s}^{-1}$. In Figure 9 the structure of the models is displayed after a quasi-steady state flow has been established. In both cases the spherically symmetrical wind emerging from the central protostar is collimated within the PDR to a bipolar outflow by the ram pressure of the neutral evaporating flow ($v\dot{M}$)_{ph}. The opening angle of the jet is proportional to the ratio $(v\dot{M})_{\text{wind}}/(v\dot{M})_{\text{ph}}$ (Yorke & Welz 1996). Since \dot{M}_{ph} is smaller below the disk the opening angle is greater than above the disk. The disk itself and the location of the C I-front are not effected but the shape of the H I-front is modified by the more powerful stellar winds. Above the disk the ram pressure of the jet $(v\dot{M})_{\text{wind}}$ is able to push the H I-front near the rotation axis toward the ionizing star. For case D $(v\dot{M})_{\text{wind}}$ is too low to change the structure of the H I-front of the tail significantly, whereas for case E the jet breaks through and the low-density wind region becomes completely ionized.

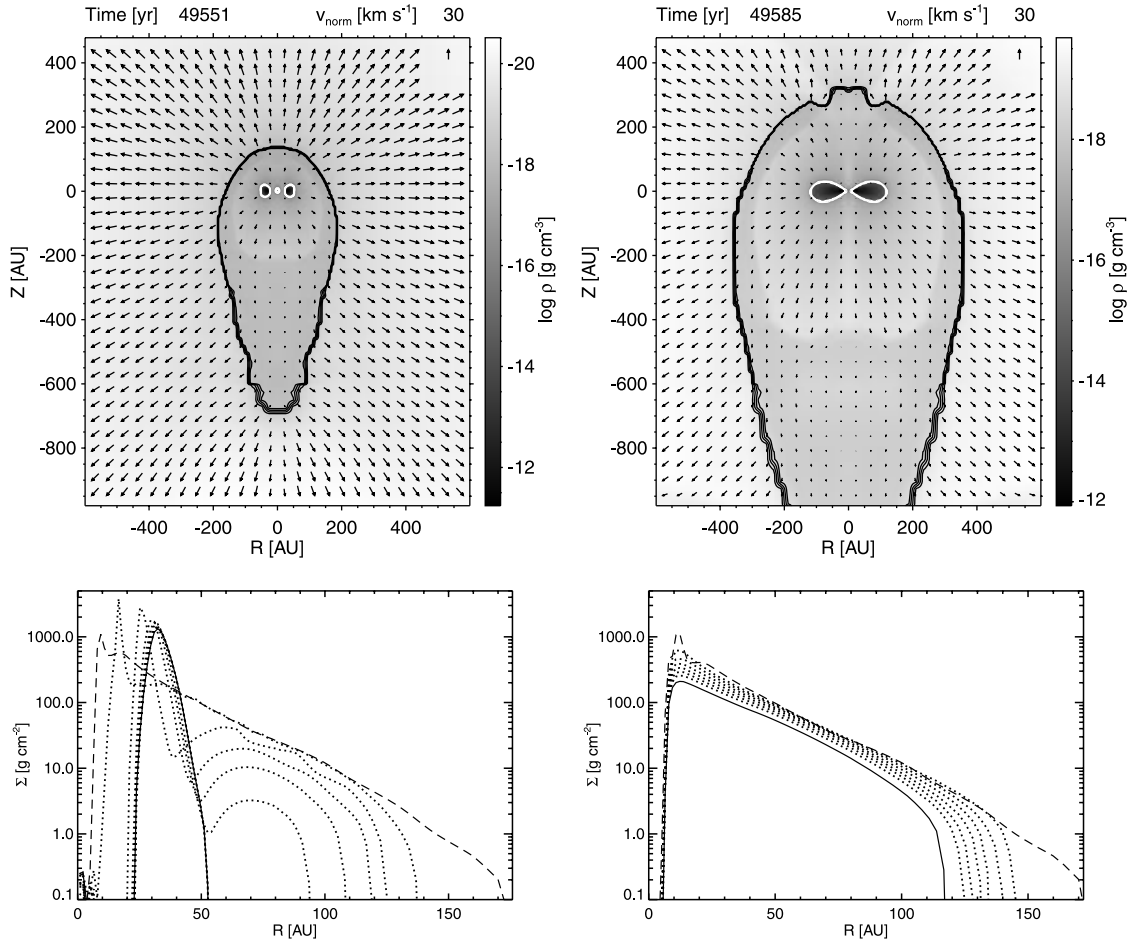


FIG. 10.—Density, I-front, and velocity structure (*top*) and the corresponding evolution of the surface density Σ (*bottom*) at the end of the simulations F (negligible angular momentum transport) and G (significant angular momentum transport). Σ is given near the begin of the simulation (*dashed lines*, $t \lesssim 100$ yr), at the end of the simulation (*solid lines*, $t = 5 \times 10^4$ yr), and at several intermediate stages (*dotted lines*, $\Delta t \sim 6 \times 10^3$ yr).

5.4. Influence of Angular Momentum Transfer (Cases F and G)

With simulation F and G we examine the importance of angular momentum transfer for the evolution of externally illuminated disks. We model angular momentum transfer

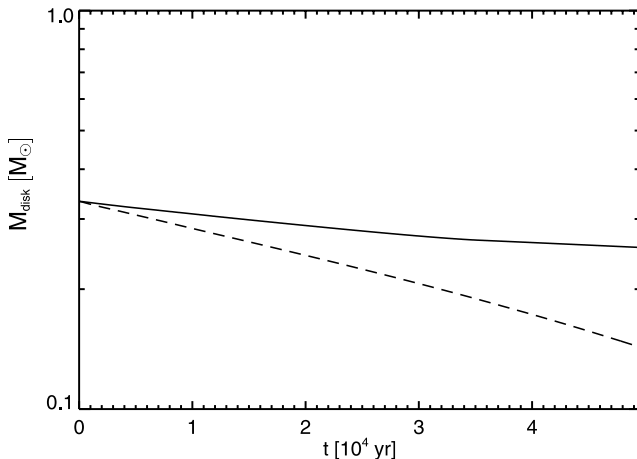


FIG. 11.—Evolution of the disk mass in simulations F (*solid line*) and G (*dotted line*).

according to an α formalism (Shakura & Sunyaev 1973): the kinematic viscosity coefficient is given by $\nu = \alpha c_s H$, where α is a dimensionless parameter, c_s the sound speed, and H the scale height of the disk. We begin these simulations with star-disk model II. The collapse simulations associated with this initial configuration implicitly assume that angular momentum transport is initiated by tidal forces due to gravitational instabilities and α is adjusted according to the value of the Toomre parameter (Yorke & Bodenheimer 1999). In contrast to model I the compact disk of model II is more unstable against nonaxisymmetric gravitational modes leading to a higher α and therefore to a higher accretion luminosity (see L_{star} in Table 1). Here we do not attempt to model a particular mechanism for the transport of angular momentum but assume a constant value for α for two extreme cases: Case F is a simulation with negligible angular momentum transfer ($\alpha = 10^{-6}$) and for case G we use $\alpha = 10^{-2}$. All other parameters are the same as for case B.

The results of both cases are shown in Figure 10. We compare the simulations at the same evolutionary times at the end of the calculations. The upper pictures show the density and velocity structure and the lower pictures the evolution of the surface density. In both cases the size of the ionized envelope is comparable to the observations even at very early stages. In case F the disk completely changes its

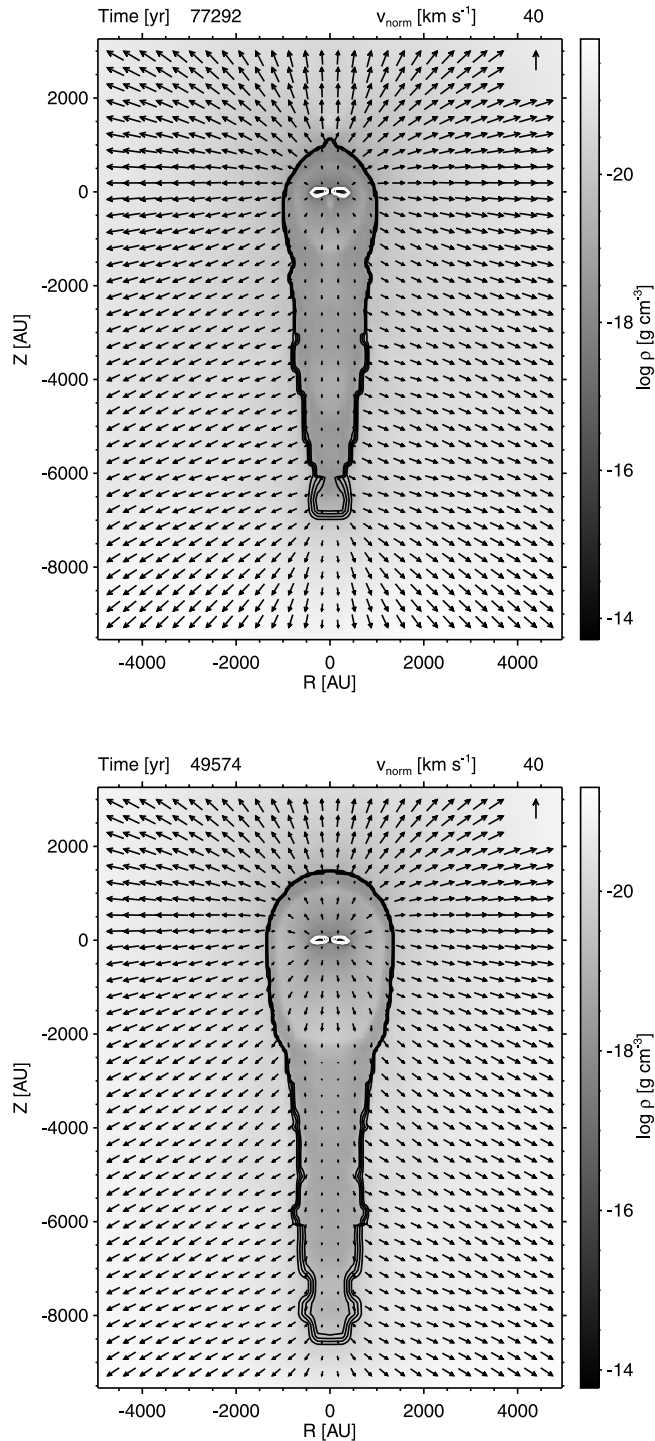


FIG. 12.—Density and velocity structure of the head-tail objects in simulations H and J at evolutionary times for which the disk radius R_C is the same.

internal structure because of the sudden decrease of angular momentum transfer. The final structure is that of a torus. Due to the low disk surface the mass of the disk decreases very slowly (Fig. 11). The evaporation timescale in case F is $t_{\text{evap}}^F = 18 \times 10^4$ yr. In case G the disk maintains its structure. As in case B the disk is photoevaporated from outside, but the slope of the surface density remains the same. The photoevaporation timescale $t_{\text{evap}}^G = 6.1 \times 10^4$ yr is about 3 times shorter than in case F. Thus, it is necessary to know

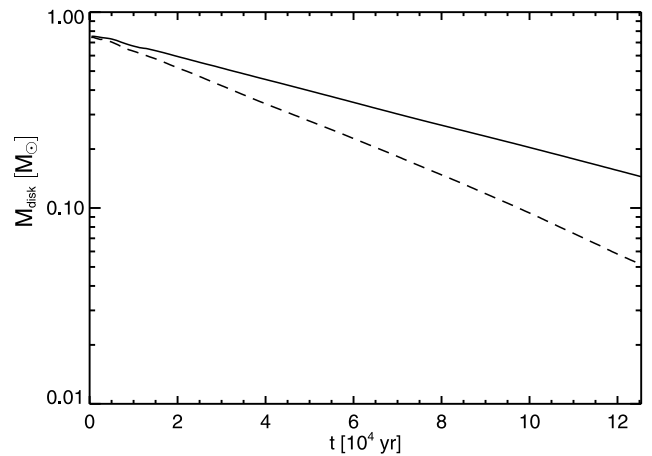


FIG. 13.—Evolution of the disk mass in simulations H (solid line) and J (dotted line).

the efficiency of angular momentum transport mechanisms to determine the lifetime of a disk in an external radiation field properly.

The torus-shaped disk at the end of simulation F resulted from a sudden change of α . Such tori occur in nature when the inner regions are cleared by a close companion, analogous to the circumbinary disk of GG Tau (Guilloteau, Dutrey, & Simon 1999). Numerical simulations of gap clearing (Larwood & Papaloizou 1997) show that circumbinary disks are truncated at a radius where viscous and tidal torques balance. The lack of viscosity in the inner regions of the disk leads to a density enhancement near the truncation radius and a steeper surface density profile, comparable to our simulation F. This implies that circumbinary disks are *less* susceptible to destruction by photoevaporation than circumstellar disks; i.e., their photoevaporation timescales are longer. Simulation F possibly overestimates this effect, however, because the assumption of zero angular momentum transfer also leads to more compact disks.

5.5. Influence of the FUV/EUV Ratio (Cases H and J)

Simulations H and J begin with star-disk model III. The initial conditions are the same for both cases except that the FUV/EUV ratio is 5 times higher for case J than for case H (Table 2). Figure 12 shows a comparison of the head-tail objects at evolutionary times with equal disk radii. For simulation J the wind-blown bubble within the PDR is greater than for case H and shows an elliptical shape. Moreover, the radius of the H I-front $R_H \sim 5 \times R_C$ and the tail length Z_{tail} are greater than for case H. The decrease in disk mass is faster for case J (Fig. 13). Accordingly, the corresponding photoevaporation timescale of case J ($t_{\text{evap}}^J = 4.8 \times 10^4$ yr) is shorter than for case H ($t_{\text{evap}}^H = 7.4 \times 10^4$ yr).

High FUV/EUV ratios are to be expected. Realistic models for stellar atmospheres (Pauldrach et al. 1998) result in FUV/EUV ratios for the cooler OB stars ($T_{\text{eff}} < 30,000$ K) which are up to 10 times higher than those calculated from equations (1) and (2) using Planck's function. In particular, this fact should have impacts on star-disk systems in the vicinity of OB clusters where less massive members provide an FUV photon excess. The FUV/EUV ratio could also be enhanced due to the increasing specific UV dust extinction coefficient κ^{ext} with photon energy. This effect is

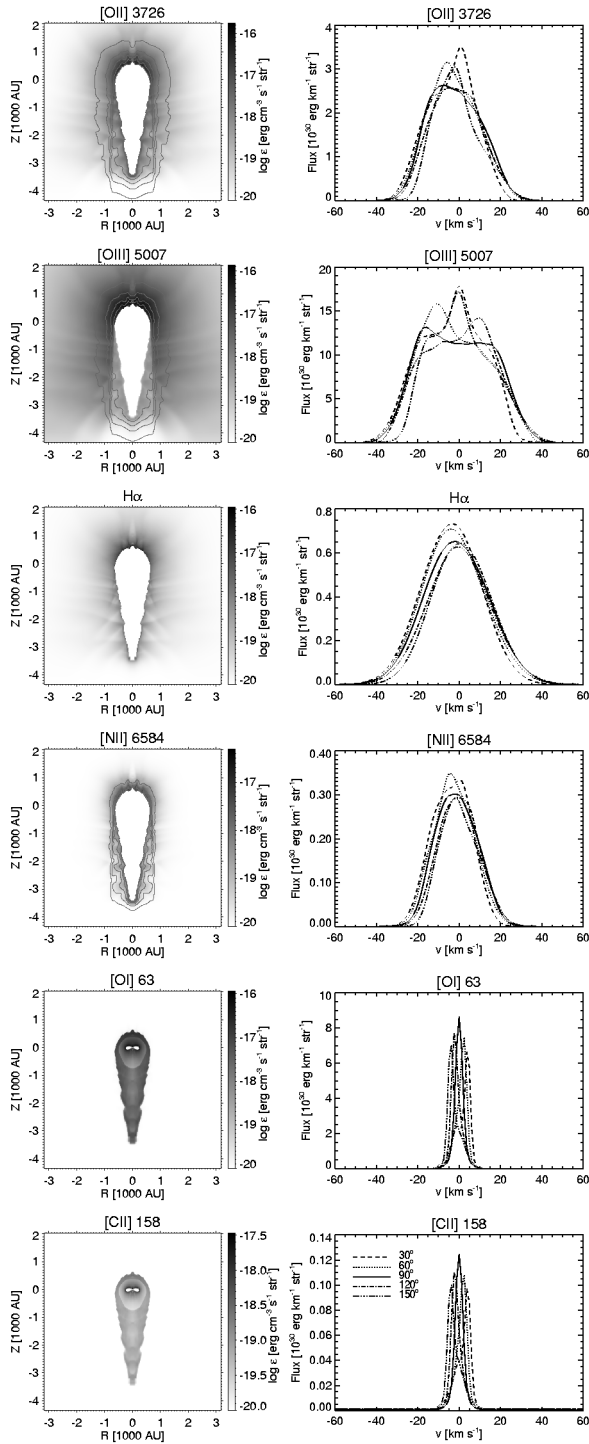


FIG. 14.—Emissivity and line profiles for the model at $t = 59,243$ yr in simulation A (Fig. 2g). The contour lines of the relevant degree of ionization are given for the values 0.2, 0.4, 0.6, and 0.8.

not considered in the simulations because the absolute value of κ^{ext} strongly depends on the dust model (Preibisch et al. 1993). Some of the Orion Nebula proplyds have large $R_H \sim 4 \times R_C$ (Bally et al. 1998a). This is not necessarily a strong indication of a high FUV/EUV ratio in the Trapezium Cluster, because R_H/R_C is also large for smaller values of R_C and larger distances to the ionizing source (see 5.2).

6. EMISSION LINE MAPS

For direct comparison with observations we use a ray-tracing code to calculate line spectra and emission line maps. The basic features of this code optimized for circumstellar disks embedded in an ionized medium are described in Kessel, Yorke, & Richling (1998). For the present investigation we use a modified version especially adapted to the case of externally illuminated disks. We examine the optical lines [O III] 5007 Å, [O II] 3726 Å, Hα, [N II] 6584 Å, and the NIR lines [O I] 63 μm and [C II] 158 μm.

Before the actual ray-tracing procedure the abundances of O II, O III, and N II are determined by solving the equation for ionization and recombination balance. The degree of ionization of hydrogen and carbon are known. For the NIR lines it is assumed that there is no contribution to the emission in regions where hydrogen is ionized. Then the code solves the rate equations to obtain the population density for the upper level n_i . The line emissivity for a transition from level i to level j is calculated from

$$\epsilon = \frac{1}{4\pi} n_i A_{ij} h\nu_{ij} \beta_{\text{esc}}(\tau_{ij}), \quad (18)$$

where A_{ij} is the spontaneous transition probability and $h\nu_{ij}$ the energy difference between level i and j . The escape probability β_{esc} is only considered for the NIR lines. The ray-tracing code itself solves the time-independent equation of radiation transfer for a nonrelativistic moving medium along lines of sight for different viewing angles. The resulting emission line maps are convolved with a Gaussian point spread function with a FWHM of 22 AU, which is comparable to the resolution of the *HST* for the distance of the Orion Nebula.

Figure 14 shows the emissivity ϵ and the calculated line profiles for case A at $t = 59,243$ yr shown in Figure 2g. In addition, for the forbidden lines of O II, O III, and N II contour lines for the relevant degrees of ionization are given. The abundance of O II is high near the H I-front and in the shadow regions ionized by diffuse EUV photons. Further outside in regions ionized by direct EUV photons O II becomes ionized and the abundance of O III increases. The emissivity of [O III] 5007 is thus more extended than the emissivity of [O II] 3726. The emissivity of Hα and [N II] 6584 is similar to that of [O II] 3726. They attain their maxima at the H I-front. The abundance of N II falls off more rapidly for the benefit of N III than the abundance of O II because the ionization potential of N II is lower than the ionization potential of O II. The emissivity of the NIR lines is strongest at the C I-front near the disk surface and in the compressed subsonic PDR regions beyond the wind-blown cavity.

The line profiles in Figure 14 are given for five different viewing angles. The viewing angle is defined as the angle between the rotation axis of the disk and the line of sight. A viewing angle of 0° means we observe the disk pole-on from the direction of the ionizing star. At a viewing angle of 90° the disk is observed edge-on. The line profiles mirror the velocity field of the ionized and neutral material. Depending on the viewing angle the forbidden lines have maxima at the blue or red wing between 5 and 20 km s⁻¹. This is most clearly visible in the [O III] line, since part of the emission comes from the accelerated ionized gas further away from the H I-front. These results are consistent with the high-resolution spectroscopy of four proplyds in the Orion

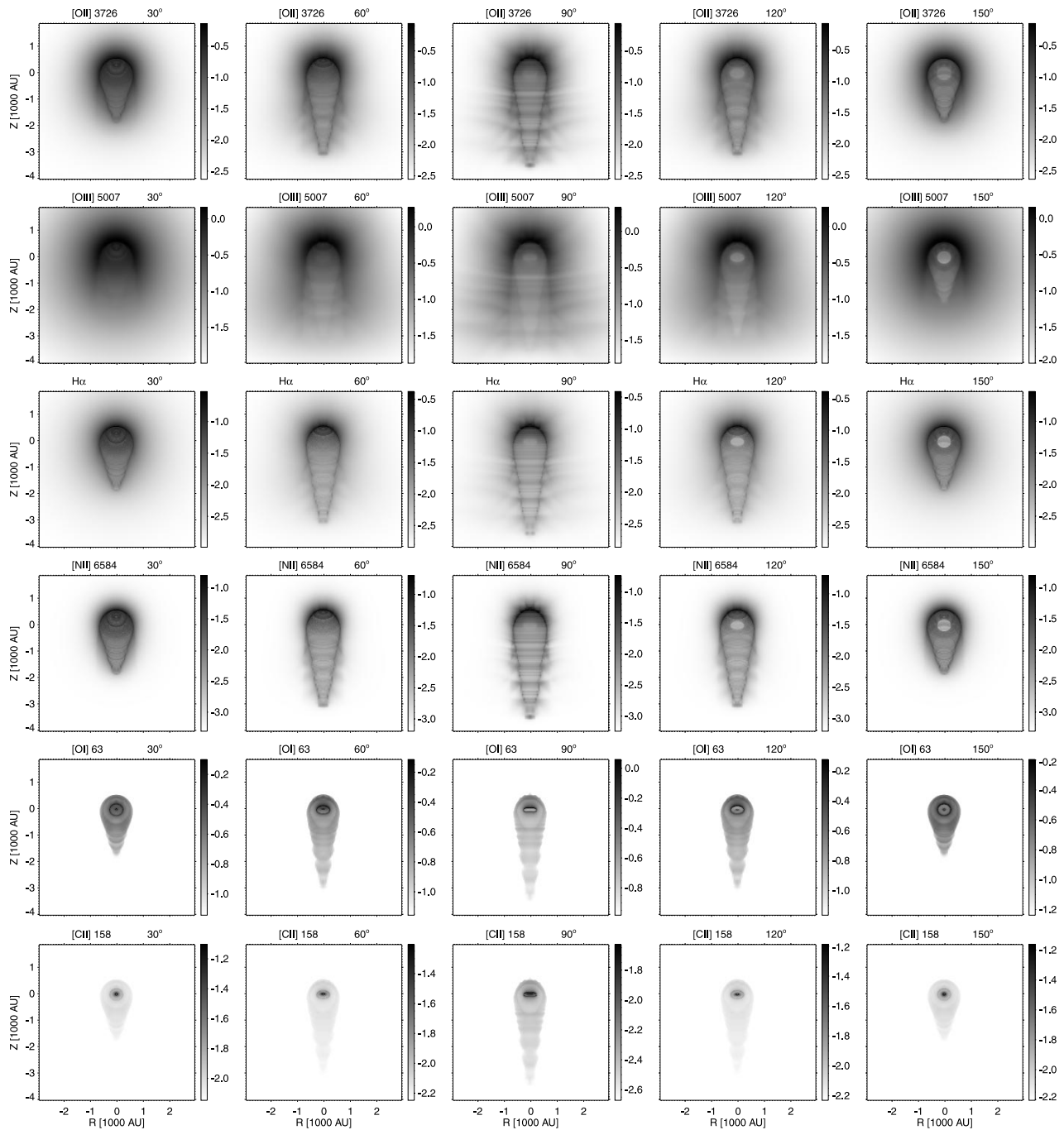


FIG. 15.—Emission line maps for the model at $t = 59,243$ yr in simulation A (Fig. 2g) for five different viewing angles. The intensity is given in $\log(I/\text{ergs s}^{-1} \text{cm}^{-2} \text{sr}^{-1})$.

Nebula by Henney & O'Dell (1999), who find a clear correlation of spectral line width with ionization potential. Due to the low atomic weight of hydrogen the broad $H\alpha$ line shows the least variation with viewing angle. The NIR lines are much narrower because they mainly trace the low velocity material near the disk surface and in the subsonic regions.

In Figure 15 the corresponding emission line maps are displayed. As expected from the emissivity distributions shown in Figure 14, the emission line maps of $[O II]$, $H\alpha$, and $[N II]$ are quite similar. The emission is brightest at the head of the object and along the tail and is thus consistent

with observations which show limb-brightened tails (Bally et al. 1998a). For viewing angles $\geq 90^\circ$ a silhouette disk is visible in the bright envelope. The $[O III]$ maps show more diffuse emission line crescents. For angles $\leq 60^\circ$ the emission is very weak in the direction of the tail. Here for angles $\geq 60^\circ$ the silhouette disk already becomes visible. For viewing angles $\geq 90^\circ$ the tail is in absorption against the diffuse emission. These results are also consistent with the observations by Bally et al. (1998a). The last two rows of Figure 15 are the emission line maps of the NIR lines $[O I]$ and $[C II]$. They show the strong emission of the warm PDR gas at the disk surface and the fainter emission

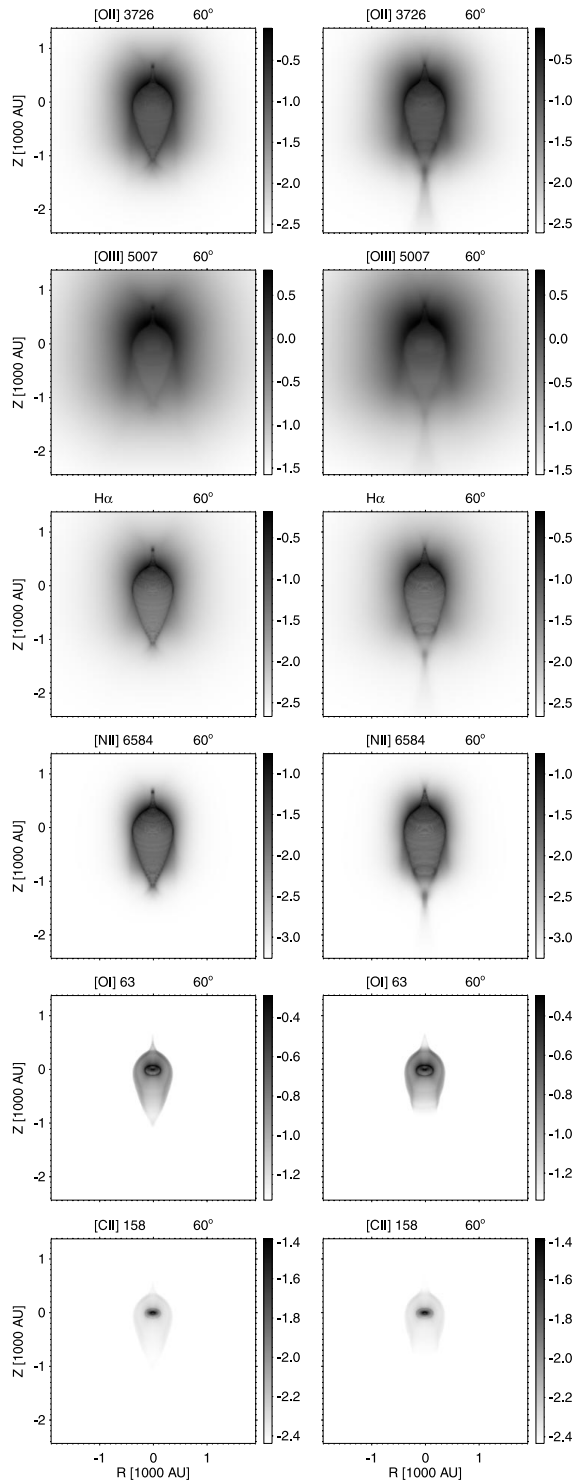


FIG. 16.—Emission line maps for the final models of cases D (right) and E (left) shown in Fig. 9.

between the H and C I-front. Although it is not yet possible to observe these lines, they will provide an important diagnostic tool for interpreting the PDRs associated with photoevaporating disks. The calculation of emission line maps of H_2 and CO that trace the molecular disk material will be included in forthcoming investigations.

Figure 16 shows the emission line maps for the models with the faster stellar winds (case D and E, see Fig. 9). The

narrow extension of the H I-front toward the ionizing source is clearly visible in the optical lines. Only for case E where the wind is strong enough to break through the H I-front can the counterjet be observed. In the NIR lines the emission in the tail is no longer visible due to the low density in the fast wind region. Stellar winds emerging from the central objects of the Orion Nebula proplyds are apparently not very powerful, since their microjets are mostly monopolar (Bally et al. 1999).

7. CONCLUSIONS

Our improved radiation hydrodynamics code is able to realistically describe the photoevaporation of circumstellar disks illuminated by external EUV and FUV sources. Despite the simplified PDR physics employed here, our results are consistent with the more elaborate PDR models by Störzer & Hollenbach (1999). In contrast to these PDR models we find several new features that are intrinsic to our self-consistent multidimensional approach.

The results of the simulations confirm that the photoevaporating disk model can explain most of the observed features of the Orion Nebula proplyds and proplyds in M8, NGC 2024, and NGC 3603. The interaction of the FUV-induced neutral flow at the disk surface with the direct and diffuse EUV radiation fields leads to the typical head-tail objects with bright emission line crescents and tails pointing away from the external radiation source. After being illuminated for times $\gtrsim 10^5$ yr, the initially rather massive disks we employ as starting models attain the masses typically observed. At this time the radius of the disk, the radius of the H I-front and the length of the tail are comparable to the observations. This is a strong indication that inferred masses and radii of observed disks significantly underestimate their values during earlier evolutionary phases and is consistent with the results of Yorke & Bodenheimer (1999) that immediately after disk formation the ratio of disk mass to star mass can be as high as 1:3 and disk radii can exceed 1000 AU.

Circumstellar disks are not necessarily seen as silhouettes in the emission line maps of proplyds, since their observability depends strongly on their orientation with respect to the ionizing sources and the observer. The [O III] emission appears more diffuse than the other emission lines considered, because the relative abundance of O III is low in the compressed regions, e.g., near the H I-front and in the shadow regions along the tail.

Monopolar and bipolar microjets emerging from the proplyds can be explained by spherically symmetric stellar winds focused by the neutral evaporating flow from the disk surface. Because of the symmetry assumed, these microjets necessarily coincide with the head-tail orientation of our simulated proplyds. With a more elaborate three-dimensional treatment a more complex flow pattern of focussed stellar winds and photoevaporation outflows will result.

If sufficient angular momentum transfer is present, the evaporation timescale is almost independent of the initial radius of the disk and consequently of the compactness of the parental molecular cloud cores. Note that this does not necessarily mean that the lifetime of protostellar disks is independent of the compactness of the cluster within which it formed (see below).

Due to our assumed face-on illumination and the fixed distance to the illuminating star the calculated evaporation

timescales yield a lower limit for the illumination timescale of 10^5 yr, which lies in the range of the observed age of the Trapezium Cluster. The evaporation timescale is influenced by angular momentum transfer and the FUV/EUV flux ratio. Within the parameter space investigated here, either mechanism can change the evaporation timescale by a factor of 2 to 3. Tidal stripping by close or penetrating encounters (Hall 1997) as well as inner disk clearing by close companions steepen the surface density profile and actually lead to more robust disks and longer evaporation timescales. In the dense Trapezium Cluster where $n_{\text{core}} = 2 \times 10^4$ stars pc^{-3} (Hillenbrand & Hartmann 1998) both effects can be expected, assuming a binary fraction comparable to the galactic field (Petr et al. 1998). Further investigations are planned to consider orbital data obtained by

N-body simulations of cluster evolution scenarios (Kroupa, Petr, & McCaughrean 1999).

This research has been supported by the Deutsche Forschungsgemeinschaft (DFG) within the framework of the “Physics of Star Formation” program under grant Yo 5/19-2 and by the National Aeronautics and Space Administration (NASA) under the auspices of the “Origins” Program and grant NRA-99-01-ATP-065. Portions of this research were conducted at Jet Propulsion Laboratory, California Institute of Technology. The calculations were performed at the John von Neumann Institute for Computing (NIC) in Jülich, the Leibniz Computing Center (LRZ) in Munich, and the Astronomical Institute in Würzburg.

REFERENCES

- Bakes, E. L. O., & Tielens, A. G. G. M. 1994, *ApJ*, 427, 822
 Bally, J., O'Dell, C. R., McCaughrean, M., & Sutherland, R. S. 1999, *BAAS*, 194, 6812b
 Bally, J., Sutherland, R. S., Devine, D., & Johnstone, D. 1998a, *AJ*, 116, 293
 Bally, J., Testi, L., Sargent, A., & Carlstrom, J. 1998b, *AJ*, 116, 854
 Bertoldi, F. 2000, *A&A*, in press
 Brandner, W., et al. 1999, *BAAS*, 194, 6808b
 Cesaroni, R., Felli, M., Jenness, T., Neri, R., Olmi, L., Robberto, M., Testi, L., & Walmsley, C. M. 1999, *A&A*, 345, 949
 Chen, H., Bally, J., O'Dell, C. R., McCaughrean, M. J., Thompson, R. L., Rieke, M., Schneider, G., & Young, E. T. 1998, *ApJ*, 492, L173
 Close, L. M., et al. 1998, *ApJ*, 499, 883
 de Jong, T., Dalgarno, A., & Boland, W. 1980, *A&A*, 91, 68
 Draine, B. T., & Lee, H. M. 1984, *ApJ*, 285, 89
 Guilloteau, S., Dutrey, A., & Simon, M. 1999, *A&A*, 348, 570
 Hall, S. M. 1997, *MNRAS*, 287, 148
 Henney, W. J., & O'Dell, C. R. 1999, *AJ*, 118, 2350
 Hillenbrand, L. A. 1997, *AJ*, 113, 1733
 Hillenbrand, L. A., & Hartmann, L. W. 1998, *ApJ*, 492, 540
 Hollenbach, D., & Tielens, A. G. G. M. 1997, *ARA&A*, 35, 179
 Hollenbach, D., Yorke, H. W., & Johnstone, D. 2000, in *Protostars & Planets IV*, ed. V. Mannings, A. P. Boss, & S. S. Russell (Tucson: Univ. Arizona Press), 401
 Johnstone, D., & Bertoldi, F. 2000, in *The Orion Complex Revisited*, ed. M. McCaughrean & A. Burkert (San Francisco: ASP), in press
 Johnstone, D., Hollenbach, D., & Bally, J. 1998, *ApJ*, 449, 758
 Kessel, O., Yorke, H. W., & Richling, S. 1998, *A&A*, 337, 882
 Körner, D. W., Ressler, M. E., Werner, M. W., & Backman, D. E. 1998, *ApJ*, 503, L83
 Kroupa, P., Petr, M. G., & McCaughrean, M. J. 1999, *NewA*, 4, 495
 Larwood, J. D., & Paploizou, J. C. B. 1997, *MNRAS*, 285, 288
 Levermore, C., & Pomraning, G. 1981, *ApJ*, 248, 321
 Mannings, V., & Sargent, A. I. 2000, *ApJ*, 529, 391
 McCaughrean, M. J., & Stauffer, J. R. 1994, *AJ*, 108, 1382
 Nahar, S. N., & Pradhan, A. K. 1994, *Phys. Rev. A*, 49, 1816
 O'Dell, C. R., Wen, Z., & Hu, X. 1993, *ApJ*, 410, 696
 Padgett, D. L., Brandner, W., Stapelfeldt, K. R., Strom, S. E., Terebey, S., & Körner, D. 1999, *AJ*, 117, 1490
 Pauldrach, A. W. A., Lennon, M., Hoffmann, T. L., Sellmaier, F., Kudritzki, R.-P., & Puls, J. 1998, in *ASP Conf. Ser. 131, Properties of Hot, Luminous Stars*, ed. I. Howarth (San Francisco: ASP), 258
 Petr, M. G., Du Foresto, V., Beckwith, S. V. W., Richichi, A., & McCaughrean, M. J. 1998, *ApJ*, 500, 825
 Preibisch, Th., Ossenkopf, V., Yorke, H. W., & Henning, T. 1993, *A&A*, 279, 577
 Richling, S., & Yorke, H. W. 1997, *A&A*, 327, 317
 ———. 1998, *A&A*, 340, 508
 Shakura, N. I., & Sunyaev, R. A. 1973, *A&A*, 24, 337
 Spaans, M., Tielens, A. G. G. M., van Dishoeck, E. F., & Bakes, E. L. O. 1994, *ApJ*, 437, 270
 Stapelfeldt, K. R., Krist, J. E., Menard, F., Bouvier, J., Padgett, D. L., & Burrows, C. J. 1998, *ApJ*, 502, L65
 Stecklum, B., Henning, T., Feldt, M., Hayward, T. L., Hoare, M. G., Hofner, P., & Richter, S. 1998, *AJ*, 115, 767
 Sternberg, A., & Dalgarno, A. 1995, *ApJS*, 99, 565
 Störzer, H., & Hollenbach, D. 1998, *ApJ*, 495, 853
 ———. 1999, *ApJ*, 515, 669
 Suttner, G., Yorke, H. W., & Lin, D. N. C. 1999, *ApJ*, 524, 857
 Tielens, A. G. G. M., & Hollenbach, D. 1985, *ApJ*, 291, 722
 Yorke, H. W., & Bodenheimer, P. 1999, *ApJ*, 525, 330
 Yorke, H. W., & Kaisig, M. 1995, *Comput. Phys. Commun.*, 89, 29
 Yorke, H. W., & Welz, A. 1996, *A&A*, 315, 555